Plasmonics (2024) 19:1989–1999
https://doi.org/10.1007/s11468-023-02130-2

RESEARCH

Extraordinary Optical Transmission Spectrum Property Analysis of Long-Wavelength Infrared Micro-Nano-Cross-Linked Metamaterial Structure

Peng Sun[1] · Hongxing Cai[1] · Yu Ren[1] · Jianwei Zhou[1] · Dongliang Li[1] · Teng Li[1]

Received: 25 October 2023 / Accepted: 14 November 2023 / Published online: 28 November 2023

Abstract
Filter elements based on metamaterial structure are one of the essential schemes for researching the miniaturization of spectral detection systems. The aim of this study is to meet the application requirements of different long-wave infrared signal frequency filtering and improve the detection efficiency of micro-filters. In this paper, a periodic micro-nano-cross-linked hole structure is designed, based on the surface plasmonic polariton resonance effect to realize the extraordinary optical transmission performance of 8 ~ 12 μm long-wave infrared. Based on the surface plasmonic polariton excitation mechanism of periodic micro-nano-structures, the tunable performance of the transmission spectra at five central wavelengths of 8, 9, 10, 11, and 12 μm was achieved by changing the simulation period and the overall period of the model, and the optimal peak transmittance was 88.31% with a half-wave width of 1.31 ± 0.01 μm. The present study summarizes the tuning mode and rule of the micro-nano-cross-linked structure to realize the blue/redshift under the performance of the extraordinary optical transmission, which provides an important reference for the miniaturized structure design of infrared spectral detectors and tunable filtering research and is conducive to the application of broadband filtering spectral chips.

Keywords Transmission spectroscopy · Metamaterials · Surface plasmonic polaritons · Micro-nano-optics

Introduction

With the rapid growth of the application space of spectrum analysis, the subject of miniaturization of spectral detector devices has become one of the research hotspots in the field of spectral technology [1]. The manipulation and adjustment of light by adjusting the structure size of electromagnetic metamaterials are an effective way to realize the miniaturization of spectral detectors [2–5]. However, there are few studies on long-wavelength infrared (LWIR) transmission optical filter. LWIR has better atmospheric transmission characteristics, and because the target itself will also radiate infrared spectra and the vast majority of molecular bonding in the band has an intrinsic mode of vibration, infrared spectral detectors are widely used in deep space exploration [6–8], camouflage identification [9–12], pathology [13–15], industrial monitoring [16, 17], and other fields.

In 1998, Ebbesen et al. first found that the transmission coefficients of periodic subwavelength metallic Ag thin-film hole arrays are many times larger than those predicted by the traditional Bethe classical diaphragm diffraction theory and named this optical phenomenon as optical extraordinary optical transmission (EOT) [18]. This led researchers to expand the study of extraordinary transmission. In 2019, Tavakoli et al. investigated different shapes of Au membrane layer hole arrays by theoretical computational simulation and analyzed the R. W. Wood EOT mechanism at 400 ~ 1400 nm [19]. In 2020, Park et al. researched the effect of triangular nano-hole structure parameter modulation on extraordinary optical transmission-induced spectral shift in the visible range [20]. In 2021, Song et al. designed a hole-embedded hemispherical structure by the simulation to realize the far-infrared EOT model at 4 ~ 6 THz [21]. To further improve the detection efficiency, study the tunable characteristics of the frequency band. In 2018, Wang et al. prepared Au hole arrays and realized transmission spectral filters with transmission peak center positions from 3.5 to

✉ Hongxing Cai
caihx@cust.edu.cn

Peng Sun
15140080201@163.com

[1] School of Physics, Changchun University of Science and Technology, Changchun 130022, China

approximately 13.5 μm by increasing the array period size [22]. In 2021, Lee et al. designed Al disk arrays and realized multi-period filter arrays with transmission-blocking band centers at wavelengths ranging from 2.5 to approximately 10 μm by increasing the array period size [23]. Although these researches satisfy the EOT performance of the spectral structure, they still have shortcomings, such as single transmission performance and weak tuning function.

In this research, based on the surface plasmon polariton (SPP) resonance effect [26–29], to enhance the phenomenon of EOT, we designed a LWIR filter with a periodic micro-nano-cross-linked hole structure of EOT metamaterials [30], and through the modulation and by controlling the structural design of the metamaterials to meet the plasma oscillation coupling mode of the interaction between the light and the surface of the micro-nano-metal structure, the frequency, intensity, and other propagation characteristics of the SPPs in the LWIR wavelength band can be adjusted to meet the performance requirements of the tuning of the EOT filter. At present, the research of LWIR filters mainly focuses on metal–insulator-metal micro-nano-structure absorbers [31–33]. By detecting the thermal radiation of a specific band of the target, the absorbed optical signal is converted into an electrical signal. There are few studies on LWIR transmission. The purpose of this paper is to study the micro-spectral filtering equipment, which transmits the optical signal of the target band to the underlying infrared detector of the metamaterial. Table 1 shows that in LWIR, this work has a higher transmission peak and a higher spectral bandwidth, which greatly improves the energy utilization rate of the miniature spectral filter. It provides an essential reference for designing miniaturized structures of infrared spectral detectors and researching tunable properties of filters.

Model Design and Simulation Method

The periodic metal micro-nano-structure model designed in this paper is shown in Fig. 1a which shows the hole design of the micro-nano-cross-linked structure, and Fig. 1b shows the traditional circular hole structure. h is the thickness of the metal film layer, H is the thickness of the substrate, L is the periodicity of the structure of the two arrays, R_1 is the micro-nano-cross-linked structure's hole design radius, and R_2 is the conventional circular hole. This structure takes the circular hole as the design reference and makes the circumscribed square of the circular structure. We call this circle as the center circle, then take the four vertices of the square as the center of the circle to make every circle radius equal to the radius of the center circle. The resulting graphics are hollowed-out patterns of holes.

Copper metal with good electrical conductivity as well as low cost is chosen for the upper metal layer, and semiconductor silicon is selected for the lower substrate. The refractive index database of metallic copper in this paper is derived from optical constants of Cu, Ag, and Au revisited by Babar and Weaver, published in 2015 [34]. Based on the Drude model, the relationship between the refractive index and the dielectric constant of the metal copper in the LWIR band, as well as the relationship between the real and imaginary parts of the metal dielectric constant, the relationship is calculated concerning the variation of the copper dielectric constant with electromagnetic wavelength. As shown in Fig. 2, the real and imaginary parts of the dielectric constant fit well with the FDTD model data [35].

Both unit structures use periodic boundary conditions in the x–y plane; a perfectly matched layer is used in the z-axis direction. The incident light is a planar electromagnetic wave propagating in the negative z-axis. The direction of the electric field of the incident wave is along the

Table 1 Comparison of structural design schemes of LWIR metamaterial filters

Research study	This work	Ref. [22]	Ref. [23]	Ref. [24]	Ref. [25]
Wavelength region (μm)	8 ~ 12	3 ~ 14	2.5 ~ 10	8 ~ 16	8 ~ 10
Tuning ability	Tunable	Tunable	Tunable	Untunable	Untunable
Arrangement of arrays	Square	Hexagon	Hexagon	/	Square
Model types	Holes	Holes	Discs	Grating	Discs
Peak transmission in LWIR	88.31	80.06	71.23	64.25	96.92
Full width at half maximum (μm)	1.31 ± 0.01	1.04 ± 0.19	/	/	/
Preparation technology	Standard lithography	Electron beam lithography	Nano-imprint lithography	/	Standard lithography

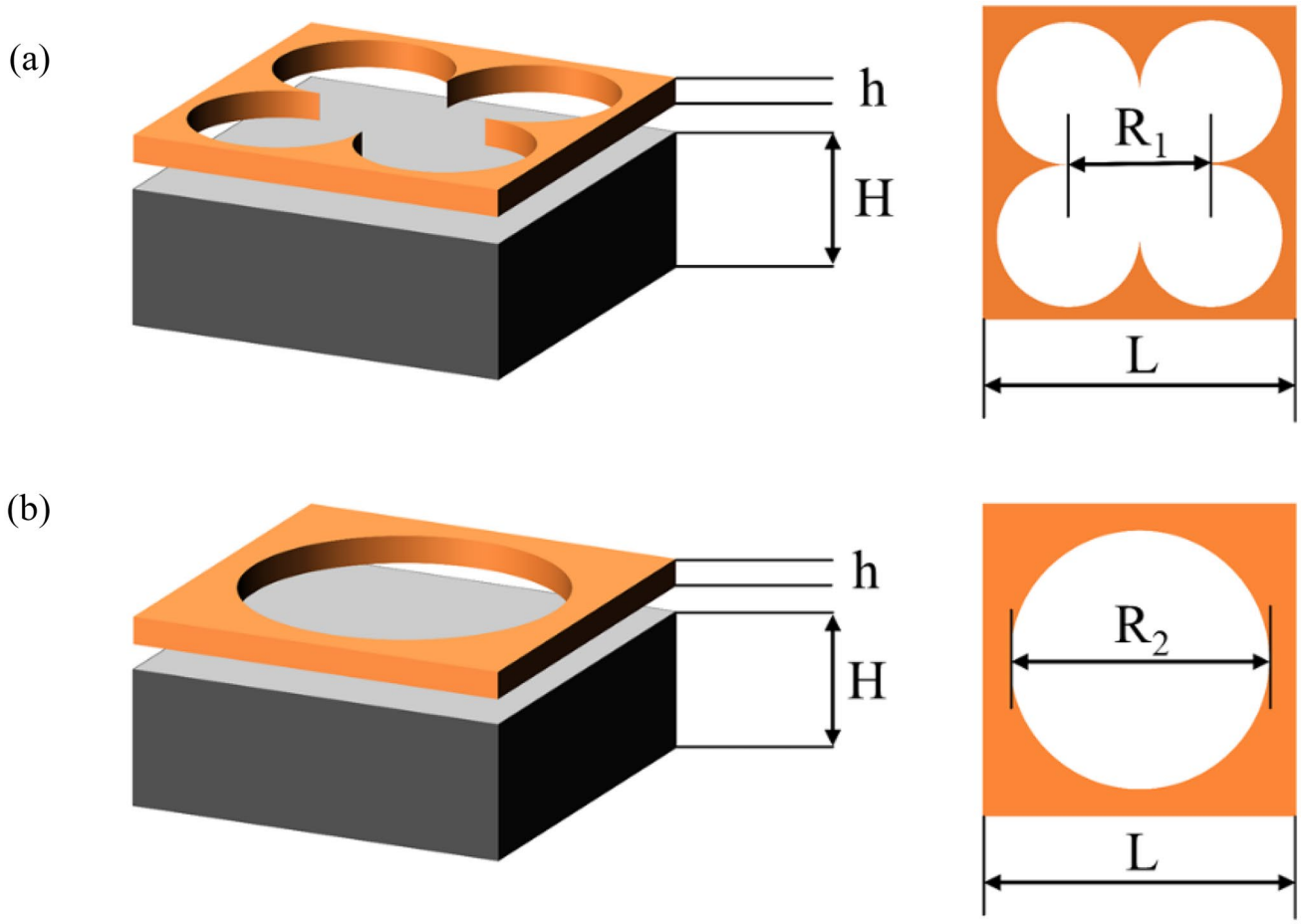

Fig. 1 Periodic metal micro-nano-structure model: **a** cross-linked hole structure; **b** traditional hole structure

x-axis, and the background on the upper surface of the metal film layer and in the holes is the air medium during the simulation. The accuracy of the mesh is set to *x*–*y* 5 nm and *z* 2 nm, respectively. Currently, the target band for the design of the EOT structure is mainly from the visible to the mid-infrared. In contrast, the LWIR metamaterial

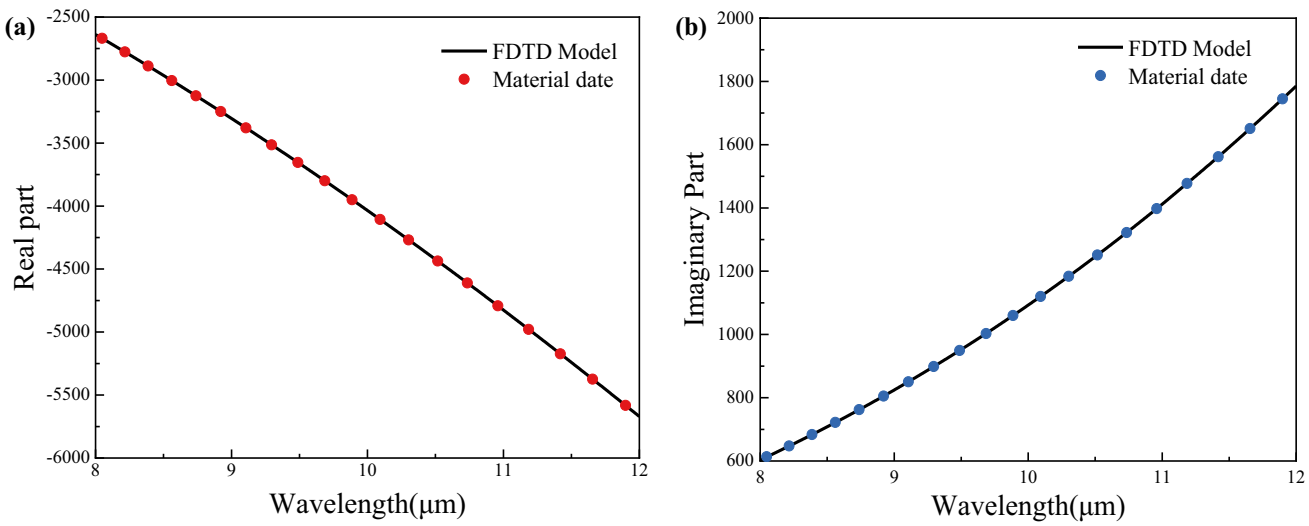

Fig. 2 Fitting of the **a** real and **b** imaginary parts of the dielectric constant of metal Cu to the FDTD model

structure is primarily a perfect absorber, which is based on the perfect absorption performance of the LWIR metal–insulator-metal structure [31–33], by eliminating its bottom metal, which is much larger than the skinning depth of incident wave designed to prevent electromagnetic wave transmission.

The dielectric constant of the free electron reaction inside the metal under the excitation of electromagnetic waves is expressed as follows:

$$\varepsilon_{(\omega)} = 1 + \chi = 1 + \frac{i\sigma_{(\omega)}}{\varepsilon_0 \omega} = 1 - \frac{\omega_p^2}{\omega^2 + i\omega\gamma_D} \tag{1}$$

The real and imaginary parts of the dielectric constant of the metal are

$$\mathrm{Re}[\varepsilon] = \varepsilon_R = 1 - \frac{\omega_p^2}{\omega^2 + \gamma_D^2} \tag{2}$$

$$\mathrm{Im}[\varepsilon] = \varepsilon_I = \omega_p^2 \gamma_D / \left[\omega\left(\omega^2 + \gamma_D^2\right)\right] \tag{3}$$

When the frequency of the incident electromagnetic wave is less than the plasma frequency, the optical frequency region $\omega_P > \omega \gg \gamma$. The real part of the dielectric constant $\varepsilon_\mathrm{R} < 0$, and the imaginary part ε_I will become extremely large, so that the incident light electric field decays rapidly inside the metal. At this time, the transverse oscillation wave is quasi-totally reflected, and there is only longitudinal oscillation of the free electron collective attenuated by single electron reception in the metal.

In addition, the internal electric field of the metal $E = E_0 \exp\left(-k\boldsymbol{k}_0 \cdot r\right)$ under the action of the electromagnetic wave of the wave vector $\boldsymbol{k}_0$; r is the displacement of the damped harmonic oscillator. The size of the excited electric field decays exponentially with the increase of the incident depth of the surface plasmon:

$$\delta_m = \frac{1}{k_0}\sqrt{\left|\frac{\varepsilon_\mathrm{I} + \varepsilon_d}{{\varepsilon_\mathrm{I}}^2}\right|} \tag{4}$$

where ε_I is the imaginary parts of the complex permittivity of the metal and, ε_d is the complex permittivity of silicon; based on formulas (3) and (4), the plasmon propagation depth of copper film in LWIR band is ~ 24 nm. In this paper, the thickness of the metal film is $h = 80 \gg \delta_m$, so the SPP mode on the upper surface of the metal film will not be directly coupled with the SPP mode on the substrate.

Due to the structural model adopting a periodic square array, the reciprocal lattice vector of its arrangement is expressed as follows:

$$u_x = \frac{2\pi}{L}x,\ u_y = \frac{2\pi}{L}y \tag{5}$$

where L is the period of the structure of the array, x and y are the unit vectors in the axial direction, respectively.

Here, we perform SPP effect analysis on an ideal circular hole [18, 36, 37]:

$$K_\mathrm{SPP} = K_\mathrm{inc} \pm nu_x + mu_y \tag{6}$$

where K_SPP is the wave vector of surface plasmonic polaritons, K_inc is the component of the incident plane wave vector on the x–y plane, and m and n are integers. For the x–y plane, under the condition of normal incidence of electromagnetic wave, $K_\mathrm{inc} = 0$. The size of K_SPP in the x-direction is $K_{\mathrm{SPP},x} = \pm n\frac{2\pi}{L}x$, and in the y-direction is $K_{\mathrm{SPP},y} = \pm m\frac{2\pi}{L}y$.

When the two diffraction waves satisfy Eq. (8), the two equal amplitude diffraction waves will propagate in the opposite direction in the x- or y-direction, resulting in their respective SPP models. Therefore, the two-dimensional SPP standing wave will be formed on the x–y plane. In the case of the fundamental mode $m = n - 1$, the period of the standing wave in the y-direction is equal to the period of the circular hole array; that is, the incident wave forms an optical lattice with the same period as the array period L above the metal film circular hole array.

The excitation wavelengths of the SPPs can be derived:

$$\lambda_\mathrm{SPPs} = L\sqrt{\frac{\left(n^2 + m^2\right)\varepsilon_1\varepsilon_2}{\varepsilon_1 + \varepsilon_2}} \tag{7}$$

where ε_1 and ε_2 are the modeled copper metal and substrate silicon dielectric constants, respectively. In the following, it is necessary to consider the wave vector matching between the micro-nano-structure and the incident electromagnetic wave during the interaction process. Wave vector is a concept that describes the spatial characteristics of the phenomenon of fluctuations, and it can be used to represent the propagation direction and speed of fluctuations. If the wave vectors of two fluctuations are the same or similar in size and converge in direction, a resonance enhancement phenomenon will occur between them. The wave vector matching condition is given by

$$k_\mathrm{SPPs} = k_0\sqrt{\frac{\varepsilon_1\varepsilon_2}{\varepsilon_1 + \varepsilon_2}} \tag{8}$$

where k_SPPs is the wave vector of surface plasmonic polaritons and k_0 is the wave vector of incident electromagnetic wave. Through the momentum conservation theorem, it can be deduced that the wave vectors of the incident light and the wave vectors of the SPPs that satisfy the wave vector matching condition have the same component perpendicular to the interface direction, which ensures that the energy of the electromagnetic wave is transferred to the SPP modes.

The micro- and nano-structures' optical properties and electromagnetic field distributions are simulated using

Ansys Lumerical FDTD software, which is mainly based on time-domain discretization and differential computation of electromagnetic wave numerical simulation methods for solving electromagnetic problems. The method is discretized in both time and space, and the propagation and interaction of electromagnetic waves are simulated and computed by solving Maxwell's system of equations and using a time-stepping algorithm.

Simulation Process and Results

Firstly, the transmission performance of these two models in Fig. 1 is simulated and compared. As shown in Fig. 3, a is the transmission spectra of the micro-nano-cross-linked structure, and b is the transmission spectra of the traditional hole structure, and after optimization of the model parameters, they both satisfy the EOT filtering performance. Much research has shown that the larger the hole area of the periodic unit structure, the more light transmission it will provide. Therefore, the simulation control by control variable method is used: the two models have the same metamaterial parameters as well as medium environment parameters, and the same hole area is set in the tuning; i.e., with the structural parameters of $R_1 = 0.5$ μm, $R_2 = 0.91$ μm, and $h = 80$ nm set, by expanding the simulation period of $L_1 = 2.40$ μm, $L_2 = 2.76$ μm, $L_3 = 3.20$ μm, $L_4 = 3.70$ μm, and $L_5 = 4.26$ μm, respectively, the transmission peaks of the micro-nano-cross-linked structure at five wavelengths $\lambda = 8$, 9, 10, 11, and 12 μm. As shown in Table 2, a comparison of the transmittance and half-peak full-width parameters of the metallic micro-nano-cross-linked structure and the conventional hole structure under the same structure duty cycle design, the localized surface plasmon resonance (LSPR) [38] main transmission peak and the plasmon resonance secondary transmission peak of the micro-nano-cross-linked structure have better transmission performance in each band, in which the transmittance of the main transmission peak is improved by 20.99% on average, and the full width at half maximum (FWHM) is improved by 0.48 ± 0.02 μm on average.

Then, the electromagnetic field distributions of these two models are comparatively analyzed. The intensity distribution of these electric fields is returned to the result in a normalized form. As shown in Fig. 4a and b, in the electric field distributions in the x–y plane of the micro-nano-cross-linked structure and the conventional hole at the $\lambda = 8.15$-μm transmission peak, the periodic metal micro-nano-cross-linked structure in a resonates at this excitation wavelength, and the two SPPs of Cu-Air and Cu-Si modes can be maximized to obtain the maximum resonance coupling effect. At the same time, the SPPs excited at the interface of the two media above and below the metal Cu will compensate for the energy loss in the hole so that the electric field inside the hole will be significantly enhanced. Ultimately, the energy of the infrared electromagnetic wave transmitted through the micro-nano-metal structure is enhanced. Compared with the other positions of the structure, the counter plot in the center region shows a dark red color, and the field strength reaches an extreme value. Meanwhile, an excellent resonant coupling effect of SPPs is also generated at the boundary center position of the structure with the adjacent micro-nano-structured cells, which will also propagate along the neighboring cells.

When transmitted to the hole, the electromagnetic wave will interact with the metal particles inside: part of the electromagnetic wave energy will be reflected and absorbed during transmission. This phenomenon is mainly affected by the inner wall of the circular arc inside the circular hole and

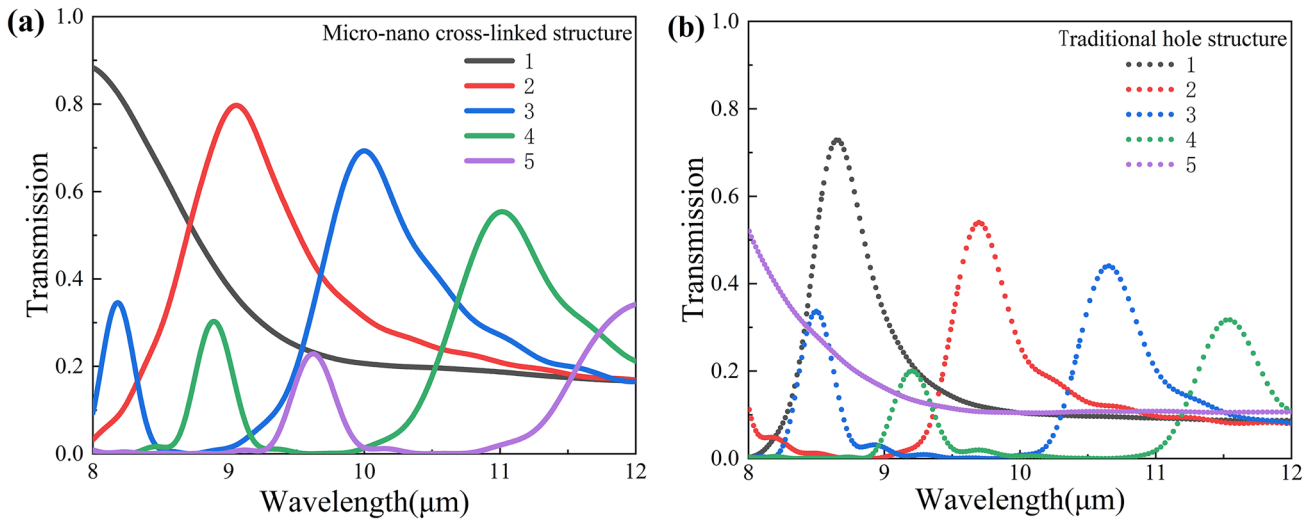

Fig. 3 Comparison of transmittance spectra of periodic **a** micro-nano-cross-linked structure and **b** traditional hole structure in 8 ~ 12 μm

Table 2 Comparison of transmittance and FWHM parameters of micro-nano-cross-linked structure and traditional hole structure

Transmission peak number	Transmission (%)		FWHM (μm)	
	Micro-nano-cross-linked structure	Traditional hole structure	Micro-nano-cross-linked structure	Traditional hole structure
1	88.31	72.92	1.31 ± 0.01	0.40 ± 0.01
2	79.69	54.01	0.78 ± 0.05	0.40 ± 0.02
3	69.30	44.08	0.94 ± 0.05	0.49 ± 0.03
3*	34.54	33.67	0.29 ± 0.01	0.26 ± 0.01
4	55.39	31.77	1.34 ± 0.05	0.65 ± 0.01
4*	30.27	20.03	0.30 ± 0.01	0.26 ± 0.01
5	34.16	19.12	0.82 ± 0.02	0.65 ± 0.02

3* and 4* are the SPP resonance peaks of the micro-nano-structure's third and fourth subtransmission spectral lines

the characteristic size of the structural tip, which changes the propagation path of the electromagnetic wave inside the hole. The other part of the electromagnetic wave may have tunnel effect [39–41]. The multiple scattering and diffraction interactions in the hole cause the excited air/Cu mode plasmon to the tunnel to the other side of the structure and propagate the energy of the electromagnetic wave to the lower surface of the metal film.

The conventional hole structure in Fig. 4b also obtains two SPP resonance modes, Cu-air and Cu-Si. Due to the different structure shapes, the excitation wavelength to satisfy the maximum resonance coupling effect is also different from that of the metallic micro-nano-cross-linked structure, and the center wavelength of its transmission peak is 8.65 μm. Because the simulation model adopts the plane wave incidence, the TM electromagnetic wave, compared with the multi-featured dimension design of the metallic micro-nano-cross-linked structure, will produce a more substantial electric field enhancement effect in the x-direction of the hole, with the extreme value of the same field strength occurring at the center of the structure. On the other hand, its electric field strength is obviously weakened in the other direction, and the whole electric field is distributed in an elliptical shape.

Figure 4c shows the normalized difference of the electric field strengths of the two structures in the x–y plane. It can be found that the periodic metal micro-nano-cross-linked structure also produces a stronger electric field enhancement

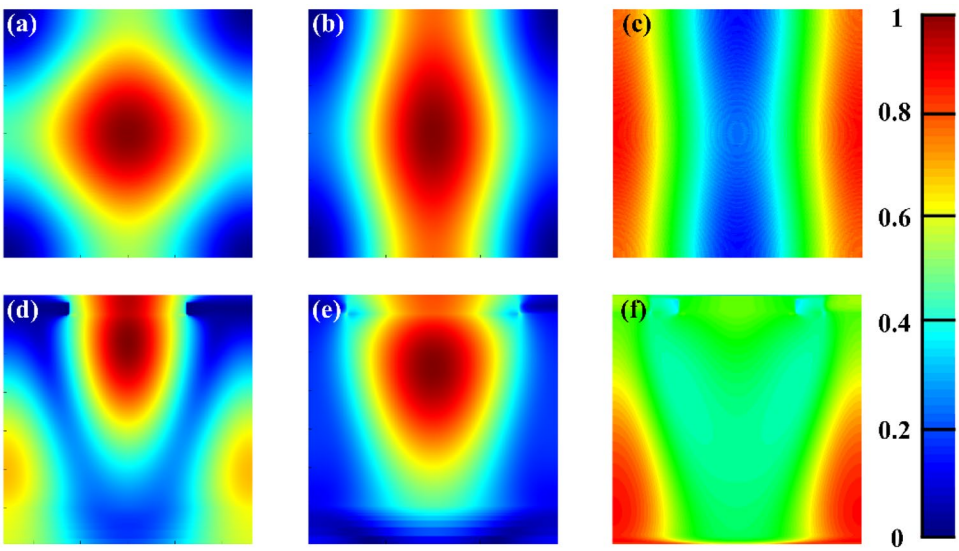

Fig. 4 Under the condition of vertical incidence. **a**, **b** The x–y plane electric field distribution of the cross-linked structure and the classical hole at the transmission peak of λ hole at the transmission peak of $\lambda = 8.15$ μm. **c** The difference between the normalized electric field strength of the x–y plane of the two structures. **d**, **e** The z-direction electric field distribution of the cross-linked structure and the classical hole at the transmission peak of $\lambda = 8.15$ μm. **f** The difference between the normalized electric field strength in the z-direction of the two structures

effect in the x-direction. The energy is slightly larger than that of the conventional hole structure. At the same time, the micro-nano-cross-linked structure obtains a significant enhancement in the y-direction on both sides. As shown in the concise schematic diagram of the transport mechanism in Fig. 5, the micro-nano-holes rely on the characteristic structural design of the combination of four circular holes to provide more efficient SPP coupling and transport enhancement in the same cell area.

Figure 4d and e shows the electric field distributions of the micro-nano-structure and the conventional hole structure in the z-direction at the $\lambda = 8.15$-μm transmission peak; it can be observed that the two structures excited air/Cu mode SPPs of each characteristic structure at the interface above the edge of the holes and at the center of the holes, respectively. When the energy is transmitted to the Cu-Si interface, it was found that the electric field energy generated by the electromagnetic wave inside the silicon dielectric was again enhanced. This is the result of the coupling of air/Cu mode and Cu/Si mode SPPs excited by the upper and lower surfaces of the metal film. At the same time, since the electrons of the metal inside the hole are affected by the oscillating electric field, the electrons that satisfy the electric field oscillation frequency will obtain enough energy to cross the hole structure barrier. This means that a part of the electrons will pass through the metal hole through the tunneling effect and escape to the other side of the hole, which in turn enhances the electric field energy of the incident electromagnetic wave propagating to the lower surface of the metal film.

Figure 4f shows the difference between the normalized electric field strengths in the z-direction of the two structures. Unlike the conventional holes, the monitor in Fig. 4d also observes the electric field enhancement effect on both sides of the micro-nano-cross-linked structure. The extreme point of the electric field strength is located below the sharp corner region formed by the two neighboring circular holes composing the micro-nano-cross-linked structure in the x-direction, i.e., in the silicon medium below the characteristic structure that generates the structure LSPR in Fig. 5. This phenomenon arises because the periodic layout of the holes induces a diffraction effect of light. According to Fraunhofer's law of diffraction, when light passes through the holes, the direction of light propagation changes, and a diffraction pattern is formed in the silicon medium. The size and distribution of the diffraction pattern will usually depend on factors such as the period and shape of the hole. Also, the edges of the holes scatter the incident electromagnetic wave. The structure has a longer pattern edge length compared to a circular hole of the same area, which will produce more scattering centers and thus change the incident electromagnetic wave vector. The incident electromagnetic wave can be further compensated because the scattered light contains some components more significant than the SPP wave vector. The feature design of the micro-nano-hole structure is more complex than that of the conventional hole structure;

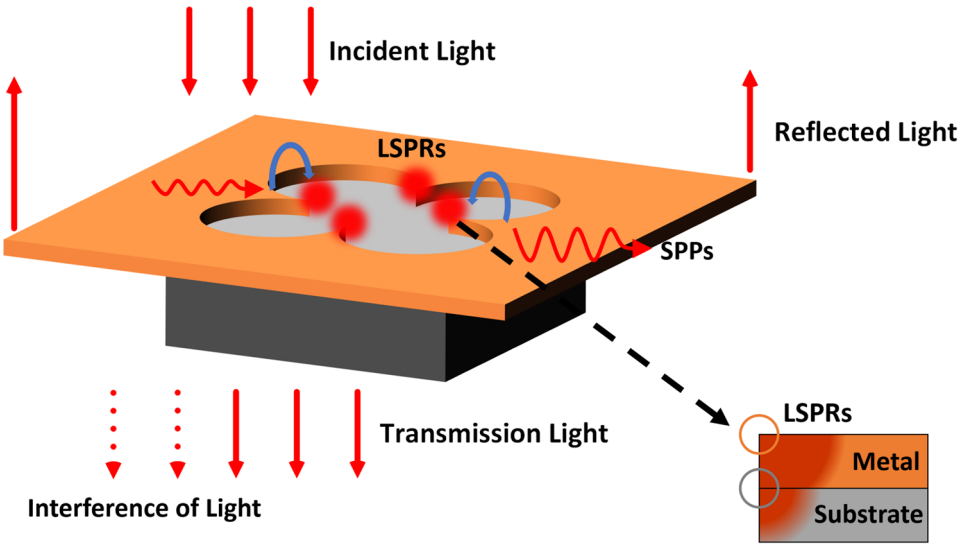

Fig. 5 Schematic diagram of the transmission enhancement mechanism in the micro-nano-cross-linked hole structure. It represents the propagation direction of the incident electromagnetic wave, and the dotted line with arrows represents the coupling effect between periodic structures. The straight line with arrows represents the propagation direction of the incident electromagnetic wave, and the dotted line with arrows represents the coupling effect between periodic structures. (The red light means the near-field optical surface enhancement effect of SPPs and LSPRs. The blue arrow indicates the coupling effect at the feature structure)

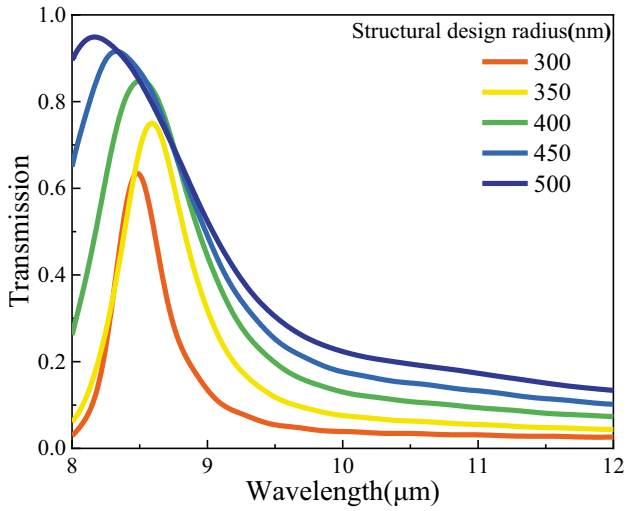

Fig. 6 In the 8 ~ 12-μm band, the relationship between the transmission spectrum of the periodic micro-nano-cross-linked structure and the design radius of the structure

thus, more interference and scattering phenomena will be induced during the transmission of electromagnetic waves.

The tunability study of the center wavelength of the transmission spectra is presented below; the relation spectra of the transmittance spectra varying with the design radius of the structure at a simulation period of 2.4 μm are shown in Fig. 6. As the design radius R_1 of the micro-nano-cross-linked structure increases, the overall transmission peak center wavelength is blueshifted, and the transmittance gradually increases. This is because a larger aperture radius allows much more light to pass through, reducing the effect of scattering due to the micro-nano-aperture structure and the material loss to the incident electromagnetic wave, which in turn increases the transmittance. In the process of increasing the design radius R_1, the structure will provide a larger effective surface area, increasing the interaction of the light field with the structure's surface and making it easier to match the excited plasma to the wavelength of the incident light. The coupling efficiency between the incident light and the free electrons in the structure is enhanced, enhancing the plasma excitation resonance strength.

Finally, in this study, the overall period of the structure is tuned under the condition that other structural parameters remain unchanged. The parameters set for the entirety period of the tuned structure are shown in Table 3, and the variation of the transmittance spectra with the overall period is shown in Fig. 7.

With the increase of the period of the structure as a whole, the tuning of the transmission peaks of the micro-nano-cross-linked structure was also realized near the five wavelengths of 8, 9, 10, 11, and 12 μm in this section of the study. According to Eq. (7), the reason for achieving the tuning is related to the excitation wavelength of the square-periodic

Table 3 Structural parameters for blueshift/redshift of periodic metal micro-/micro-nano-cross-linked structure

Transmission peak number	Center wavelength (μm)	Transmission (%)	Micro-nano-cross-linked structure characteristic parameter	
			Structural design radius (μm)	Hole period (μm)
1	8.00	88.31	0.50	2.40
2	9.08	81.51	0.60	2.90
3	9.97	74.03	0.70	3.40
4	10.94	64.03	0.88	4.20
5	11.95	33.93	1.02	4.90

array structure which is proportional to the period L; thus, the center wavelength of the transmission peak moves toward the long-wave direction as the period increases. The increase of the overall period of the structure implies the increase of the unit simulation area and the increase of the area of the structural holes. Although the hole duty cycle of the unit area is guaranteed, the spacing between the holes weakens the resonant coupling between the surfaces of the neighboring units of the structural array above the effect of the EOT, and thus, the transmittance of the main transmittance peak shows a gradually decreasing trend.

As shown in Fig. 8, increasing the overall period of the metallic micro-nano-cross-linked structure array, it can be found that the electric field strength distribution in the x–y plane undergoes a slight weakening in the x-direction

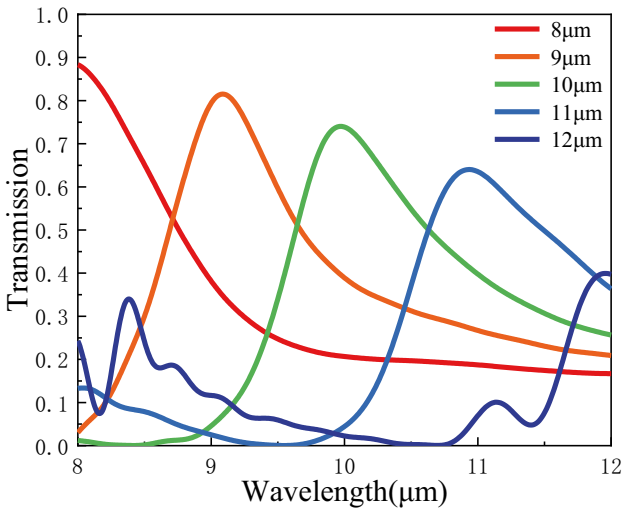

Fig. 7 In the 8 ~ 12-μm band, the relationship between the transmission spectrum of the micro-nano-cross-linked structure and the periodic of the entirety structure and the relationship between the transmittance spectral lines of the tuned micro-nano-cross-linked array period are shown

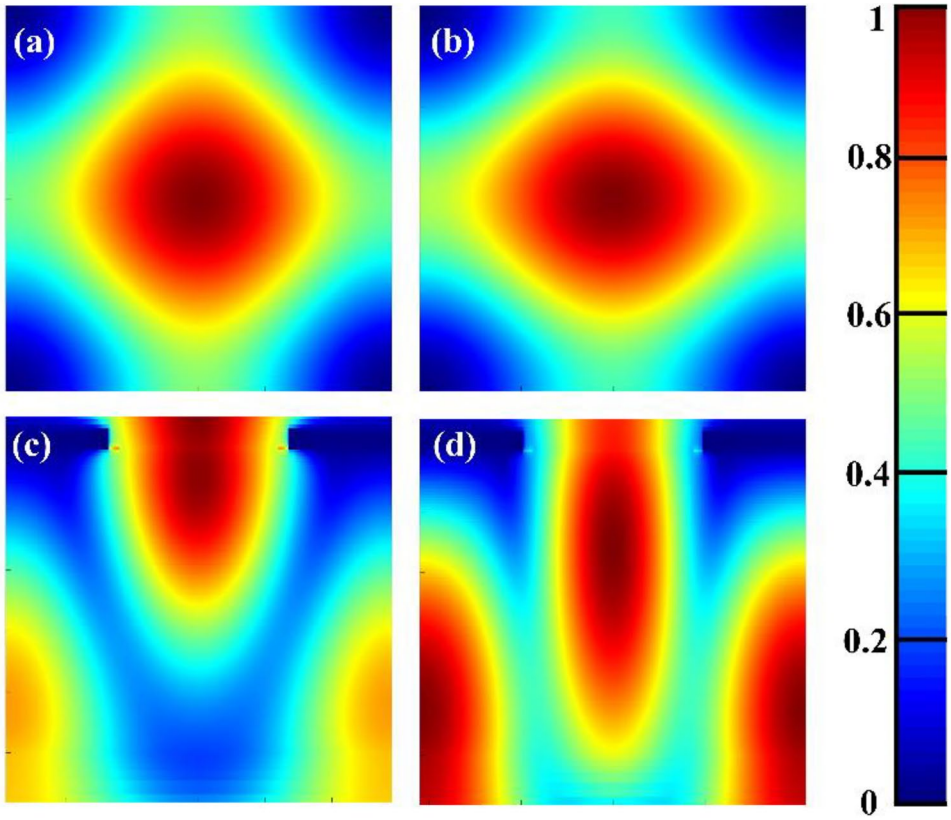

Fig. 8 Tuning the overall period of the micro-nano-cross-linked structure array. **a**, **c** $a = 2.90$ μm, $R_1 = 0.60$ μm, $\lambda = 9.08$-μm transmission peak at the micro-nano-structure x–y plane and z-direction electric field distribution; **b**, **d** $a = 4.20$ μm, $R_1 = 0.88$ μm, $\lambda = 10.94$-μm transmission peak at the micro-nano-structure x–y plane and z-direction electric field distribution

and acquires a slight enhancement in the y-direction; in the z-direction, the electric field strengths underneath the apertures and underneath the featured structure of the LSPR in Fig. 5 acquire an enhancement. This is because the change of the period and the radius of the holes affects the individual and multi-level resonance modes of the hole structure, which modifies the coupling effect of the light field in the unit structure to the electrons in the metal film layer and weakens the surface plasmonic polaritons resonance coupling effect between the individual holes. The increase in the overall period of the array also leads to the increase in the size of the characteristic structure of the LSPR so that the surface plasmonic polariton resonance effect at the tip position obtains a significant enhancement. At the same time, the feature design of the micro- and nano-aperture structures also enhances the diffraction effects of the structures, leading to a wider diffracted light spot. These diffraction effects will also affect light's propagation direction and energy distribution [42].

According to the above results, the whole extraordinary optical transmission effect is divided into five processes: (1) SPP mode of air/Cu interface, (2) LSP energy aggregation effect at the characteristic structure, (3) tunnel effect in the hole, (4) SPP mode of Cu/Si interface, and (5) array effect of micro-nano-hole structure.

According to the tuning of the transmission peak achieved by the simulation period, the structural design radius and the period of the structure respectively in Figs. 3, 6, and 7, we integrate the transmission peak tuning spectrum of the micro-nano-cross-linked metamaterials in the LWIR as shown in Fig. 9 and give the structural design parameters in Table 4.

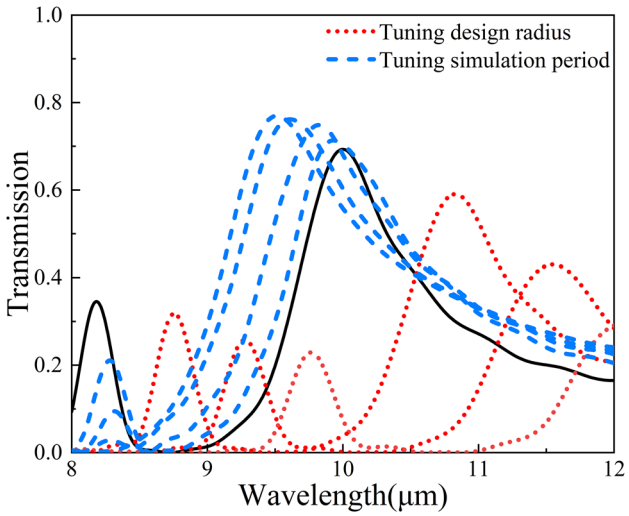

Fig. 9 The transmission peak tuning spectrum of the micro-nano-cross-linked structure in the LWIR band. The blue spectral line is tuned by controlling the radius of the structure design; the red spectral line is tuned by controlling the periodic radius of the structure. The blue spectral line is tuned by controlling the radius of the structure design; the red spectral line is tuned by controlling the periodic radius of the structure

Table 4 Structural parameters for blueshift/redshift of periodic micro-nano-cross-linked structure

Tuning trend	Performances and parameters		
	Center wavelength (μm)	Radius of the structure design (nm)	Simulation period (μm)
Blueshift	9.51	700	3.20
	9.62	650	3.20
	9.82	600	3.20
	9.93	550	3.20
Redshift	10.00	500	3.20
	10.83	500	3.60
	11.55	500	4.00
	12.00	500	4.40

Table 4 shows the transmission peaks of periodic metal micro-nano-structure LWIR corresponding to different structural design parameters. The overall tuning trend is divided into redshift and blueshift and is distinguished by color in Fig. 9. In summary, we can find the tuning law of the transmission peaks of the micro-nano-cross-linked structure in the LWIR band. Tuning the design radius of the structure will lead to the center wavelength moving to the short-wave direction, while the transmittance of the structure increases with the increase of the hole duty cycle; tuning the simulation period will lead to the center wavelength moving to the long-wave direction, while the transmittance of the structure decreases. Therefore, we can obtain the optimal transmittance performance at this location by tuning the simulation period of the structure and the radius of the structure design. Therefore, this study can realize the modulation function of any transmission spectral line under the LWIR band, which provides theoretical and data support for designing multi-channel aperture array filter structures.

Based on the above research on the spectral characteristics of the micro-nano-cross-linked structure in LWIR, the minimum feature size of this structure is a circular structure with a diameter of 1 μm. After investigation, the standard lithography process can meet the preparation requirements. For the periodic multi-size structure design in this paper, in order to meet the performance requirements of different frequency bands and low-cost batch preparation, in the subsequent work, we plan to use lithography mask preparation and lift-off process for structure fabrication.

Conclusion

This paper focuses on the characterization of the spectra of LWIR EOT metamaterials. Firstly, compared with the traditional periodic metal circular hole structure, a periodic metal micro-nano-cross-linked hole structure is designed, with an average enhancement of 20.99% in peak transmission and 0.48 ± 0.02 μm in half-wave width, which provides an important reference for the structural design of miniaturized infrared spectral detectors. Secondly, based on the parameters of the simulation period, structural design radius, and overall period of the structure, the important index of tunability in 8 ~ 12 μm LWIR EOT spectra is realized, further improving the detection efficiency of LWIR spectral devices. Finally, the modulation law of this structure is summarized: expanding the design radius to achieve a blueshift and expanding the simulation period to achieve a redshift. It can realize the modulation function of any transmission spectral line under the LWIR band. The subsequent research will mainly focus on the micro-nano-fabrication process to prepare micro-nano-structured spectral filter devices to promote the application of infrared spectral chips further.

Author Contribution All authors contributed to the study conception and design. Structural design, data collection and analysis were performed by Peng Sun, Hongxing Cai, Yu Ren, Jianwei Zhou, Dongliang Li. The first draft of the manuscript was written by Peng Sun and all authors commented on previous versions of the manuscript.

Funding This work was supported by the Natural Science Foundation of Jilin Province (20200201257JC).

Data Availability Data underlying the results presented in this paper are not publicly available at this time but may be obtained from the authors upon reasonable request.

Declarations

Ethics Approval Not applicable.

Consent to Participate Not applicable.

Consent for Publication Not applicable.

Competing Interests The authors declare no competing interests.

References

1. Yang Z, Albrow-Owen T, Cai W et al (2021) Miniaturization of optical spectrometers[J]. Science 371(6528):eabe0722. https://doi.org/10.1126/science.abe0722
2. Hu X, Zhou L, Wu X et al (2023) Review on near-field detection technology in the biomedical field[J]. Advanced Photonics Nexus 2(4):044002–044002
3. Qian J, Cao Y, Bi Y et al (2023) Structured illumination microscopy based on principal component analysis[J]. eLight 3(1):4
4. Zhang Y, He Y, Wang H et al (2020) Ultra-broadband mode size converter using on-chip metamaterial-based Luneburg lens[J]. ACS Photonics 8(1):202–208
5. Agarwal S, Prajapati YK (2018) Design of broadband absorber using 2-D materials for thermo-photovoltaic cell application[J]. Opt Commun 413:39–43
6. Irwin PGJ, Dobinson J, James A et al (2023) Spectral determination of the colour and vertical structure of dark spots in

Neptune's atmosphere. Nat Astron. https://doi.org/10.1038/s41550-023-02047-0
7. Lustig-Yaeger J, Fu G, May EM et al (2023) A JWST transmission spectrum of the nearby Earth-sized exoplanet LHS 475 b. Nat Astron. https://doi.org/10.1038/s41550-023-02064-z
8. Baqué M et al (2022) Biosignature stability in space enables their use for life detection on Mars. Sci Adv 8:eabn7412. https://doi.org/10.1126/sciadv.abn7412
9. Zhou Y, Feng H, Li X et al (2023) Tunable mid-infrared selective emitter with thermal management for infrared camouflage[J]. Plasmonics pp 1–9. https://doi.org/10.1007/s11468-023-01955-1
10. Xi W, Lee YJ, Yu S et al (2023) Ultrahigh-efficient material informatics inverse design of thermal metamaterials for visible-infrared-compatible camouflage. Nat Commun 14:4694. https://doi.org/10.1038/s41467-023-40350-6
11. Hossain MA (2023) UV–Visible–NIR camouflage textiles with natural plant based natural dyes on natural fibre against woodland combat background for defence protection. Sci Rep 13:5021. https://doi.org/10.1038/s41598-023-31725-2
12. Li M et al (2020) Manipulating metals for adaptive thermal camouflage. Sci Adv 6:eaba3494. https://doi.org/10.1126/sciadv.aba3494
13. Hua X, Wang Y, Wang S et al (2022) Ultra-compact snapshot spectral light-field imaging. Nat Commun 13:2732. https://doi.org/10.1038/s41467-022-30439-9
14. Zhang W, Suo J, Dong K et al (2023) Handheld snapshot multispectral camera at tens-of-megapixel resolution. Nat Commun 14:5043. https://doi.org/10.1038/s41467-023-40739-3
15. Zhao Y, Kusama S, Furutani Y et al (2023) High-speed scanless entire bandwidth mid-infrared chemical imaging. Nat Commun 14:3929. https://doi.org/10.1038/s41467-023-39628-6
16. Bao F, Wang X, Sureshbabu SH et al (2023) Heat-assisted detection and ranging. Nature 619:743–748. https://doi.org/10.1038/s41586-023-06174-6
17. Bannon D (2009) Cubes and slices Nature Photon 3:627–629. https://doi.org/10.1038/nphoton.2009.205
18. Ebbesen T, Lezec H, Ghaemi H et al (1998) Extraordinary optical transmission through sub-wavelength hole arrays. Nature 391:667–669. https://doi.org/10.1038/35570
19. Tavakoli M, Jalili YS, Elahi SM (2019) Rayleigh-Wood anomaly approximation with FDTD simulation of plasmonic gold nanohole array for determination of optimum extraordinary optical transmission characteristics[J]. Superlattices Microstruct 130:454–471. https://doi.org/10.1016/j.spmi.2019.04.035
20. Park J, Lee H, Gliserin A et al (2020) Spectral shifting in extraordinary optical transmission by polarization-dependent surface plasmon coupling. Plasmonics 15:489–494. https://doi.org/10.1007/s11468-019-01058-w
21. Song J, Shi Y, Liu X et al (2021) Enhanced broadband extraordinary terahertz transmission through plasmon coupling between metal hemisphere and hole arrays[J]. Optical Materials Express 11(8):2700–2710. https://doi.org/10.1364/ome.430500
22. Wang A, Dan Y (2018) Mid-infrared plasmonic multispectral filters[J]. Sci Rep 8(1):11257. https://doi.org/10.1038/s41598-018-29177-0
23. Lee HS, Hwang GW, Seong TY et al (2021) Design of mid-infrared filter array based on plasmonic metal nanodiscs array and its application to on-chip spectrometer[J]. Sci Rep 11(1):12218. https://doi.org/10.1038/s41598-021-91762-7
24. Luo Y, Liu J, Yang H et al (2023) Enhanced circular dichroism by F-type chiral metal nanostructures[C]//Photonics. MDPI 10(9):1028
25. Liu Q, Song Y, Zeng P et al (2020) High-fidelity fabrication of plasmonic nanoholes array via ion-beam planarization for extraordinary transmission applications[J]. Appl Surf Sci 526:146690
26. Zhong Y, Sun F, Liu H (2019) Impact of propagative surface plasmon polaritons on the electromagnetic enhancement by localized gap surface plasmons between metallic nanoparticles and substrate. Plasmonics 14:1393–1403. https://doi.org/10.1007/s11468-019-00929-6
27. Kolwas K (2019) Decay dynamics of localized surface plasmons: damping of coherences and populations of the oscillatory plasmon modes. Plasmonics 14:1629–1637. https://doi.org/10.1007/s11468-019-00958-1
28. Krzemińska Z, Jacak JE, Jacak WA (2023) On damping of plasmons and plasmon-polaritons in metallic nanostructures and its influence onto numerical simulations. Plasmonics 18:1211–1222. https://doi.org/10.1007/s11468-023-01838-5
29. Indhu AR, Dharanya C, Dharmalingam G (2023) Plasmonic copper: ways and means of achieving, directing, and utilizing surface plasmons. Plasmonics. https://doi.org/10.1007/s11468-023-02034-1
30. Sbeah ZA, Adhikari R, Sorathiya V et al (2023) A review on metamaterial sensors based on active plasmonic materials. Plasmonics 18:1619–1638. https://doi.org/10.1007/s11468-023-01904-y
31. Ogawa S, Kimata M (2018) Metal-insulator-metal-based plasmonic metamaterial absorbers at visible and infrared wavelengths: a review[J]. Materials 11(3):458. https://doi.org/10.3390/ma11030458
32. Luo Y, Liang Z, Meng D et al (2019) Ultra-broadband and high absorbance metamaterial absorber in long wavelength Infrared based on hybridization of embedded cavity modes[J]. Opt Commun 448:1–9. https://doi.org/10.1016/j.optcom.2019.04.080
33. Zhou Y, Qin Z, Liang Z et al (2021) Ultra-broadband metamaterial absorbers from long to very long infrared regime. Light Sci Appl 10:138. https://doi.org/10.1038/s41377-021-00577-8
34. Babar S, Weaver JH (2015) Optical constants of Cu, Ag, and Au revisited[J]. Appl Opt 54(3):477–481. https://doi.org/10.1364/AO.54.000477
35. Moharam MG, Gaylord TK (1981) Rigorous coupled-wave analysis of planar-grating diffraction[J]. JOSA 71(7):811–818. https://doi.org/10.1364/JOSA.71.000811
36. García-Vidal FJ, Lezec HJ, Ebbesen TW et al (2003) Multiple paths to enhance optical transmission through a single subwavelength slit[J]. Phys Rev Lett 90(21):213901
37. Yang F, Sambles JR (2002) Resonant transmission of microwaves through a narrow metallic slit[J]. Phys Rev Lett 89(6):063901
38. Shahnavaz N, Mohebbi M (2021) The large near-field enhancement due to strong coupling between the LSP on the metal coupled nanodisks and on the gold film for short attosecond pulse generation. Plasmonics 16:305–314. https://doi.org/10.1007/s11468-020-01340-2
39. Della Giovampaola C, Engheta N (2016) Plasmonics without negative dielectrics[J]. Phys Rev B 93(19):195152
40. Silveirinha M, Engheta N (2006) Tunneling of electromagnetic energy through subwavelength channels and bends using ε-near-zero materials[J]. Phys Rev Lett 97(15):157403
41. Li Z, Sun Y, Sun H, Wang K, Song J, Liu L, Chen X, Gu C (2017) Spoof surface plasmons tunneling through an epsilon-near-zero material channel. J Phys D Appl Phys 50(375105):7
42. Mokhtarpour R, Badri Ghavifekr H (2022) Design and optimization of surface plasmonic sensor with tunable optical actuation angle based on microsystem technology for microfluidic application. Plasmonics 17:2131–2140. https://doi.org/10.1007/s11468-022-01696-7